APL Materials

Thermodynamic investigation of phase transformation in Sn anode for magnesium batteries

Cite as: APL Mater. **10**, 071104 (2022); https://doi.org/10.1063/5.0087046
Submitted: 31 January 2022 • Accepted: 13 June 2022 • Published Online: 05 July 2022

Smobin Vincent, David Kleiven, Juan Maria Garcia Lastra, et al.

Thermodynamic investigation of phase transformation in Sn anode for magnesium batteries

Cite as: APL Mater. 10, 071104 (2022); doi: 10.1063/5.0087046
Submitted: 31 January 2022 • Accepted: 13 June 2022 •
Published Online: 5 July 2022

Smobin Vincent,[1] David Kleiven,[2] Juan Maria Garcia Lastra,[1] and Jin Hyun Chang[1,a)]

AFFILIATIONS

[1] Department of Energy Conversion and Storage, Technical University of Denmark, DK-2800 Kgs. Lyngby, Denmark
[2] Department of Physics, Norwegian University of Science and Technology (NTNU), Trondheim NO-7491, Norway

Note: This paper is part of the Special Topic on Abundant and Non-toxic Materials for Batteries.
[a)] **Author to whom correspondence should be addressed:** jchang@dtu.dk

ABSTRACT

Metallic Mg anodes are incompatible with conventional electrolytes, such as $Mg(BF_4)_2$ or $Mg(ClO_4)_2$, due to the formation of a passivation layer that blocks the transport of Mg ions, thus limiting the selection of electrolytes and cathodes. Alloying anode materials for Mg batteries, such as Sn and its intermetallics, have recently been proposed as a new class of anode materials for Mg-ion batteries to address the issues of incompatibility with the conventional electrolytes. However, the large changes in the volume of the Mg–Sn alloy during cycling lead to poor Coulombic efficiency and rapid capacity degradation. The underlying reasons for how the structural changes hamper electrochemical performance remain unclear. In this work, we perform a theoretical study of the Mg–Sn alloys to have a deeper insight into the alloying process and the phase transformation in the Sn anode. This work is the first in-depth computational study that combines density functional theory and cluster expansion to investigate the phase transition process in the Mg–Sn system that includes Mg_2Sn, α-Sn, and β-Sn structures. We considered three possible routes for the transformation pathway from Mg_2Sn to β-Sn: $Mg_2Sn \rightarrow \alpha\text{-Sn} \rightarrow \beta\text{-Sn}$, $Mg_2Sn \rightarrow \beta\text{-Sn}$, and $Mg_2Sn \rightarrow$ amorphous phase $\rightarrow \beta$-Sn. Our study shows that the transformation of Sn between its α- and β-phases hinders the alloying process. This hindrance, together with the amorphization of the alloy, is revealed to be the key factor to understand the poor electrochemical performance of the Mg–Sn alloy.

I. INTRODUCTION

Li-ion batteries (LIBs) are currently the dominant energy storage technology used in electric vehicles and portable electronic devices. LIBs still face challenges in meeting future energy storage requirements due to limited mineral resources (e.g., Li and Co) that could lead to an increase in prices and geopolitical tensions.[1–4] As a result, next-generation batteries based on naturally abundant materials are in demand, driving current research toward alternative battery chemistries. Rechargeable magnesium batteries (RMBs) are one of the promising post-Li-ion batteries. Mg is abundant in nature and safe for the environment. The divalent Mg^{2+} cations give an attractive theoretical volumetric energy density of 3833 mA h/ml,[5] which is around two times that of Li. Metallic Mg can be used as an anode for RMBs since it does not suffer from the dendrite formation[6–8] problem that affects the usage of metallic Li anodes in lithium batteries.

The metallic Mg anode suffers from two major limitations. The first issue is the incompatibility of the metallic Mg anode with conventional electrolytes, such as $Mg(BF_4)_2$ or $Mg(ClO_4)_2$; a passivation layer that forms at the electrode–electrolyte interface blocks the transport of Mg ions, preventing reversible plating and stripping from taking place.[9,10] The passivating layer consists of insoluble magnesium salts/halides formed as a reaction product of metal Mg and anions, such as ClO_4 and BF_4,[11] which got deposited on the Mg anode surface. The formation of the Mg-ion-blocking passivating layers can be prevented by using electrolytes with tetrahydrofuran (THF) and Grignard Mg salts, although they can only be operated within a narrow electrochemical window,[10,12,13] limiting the use of many high-voltage cathode materials. The second limitation of the

Mg anode is the brittleness of the Mg metal, which makes it difficult to be drawn into thin foils to be used as an anode in battery applications. Lightly doped Mg alloys can increase the ductility, but care should be given to ensure that the added dopants do not adversely affect the electrochemical properties.[14]

The alloying anode materials for Mg batteries, such as Sn,[15] In,[16] Pb,[17] Bi,[18] and their intermetallics, have recently been proposed as a new class of anode materials for Mg-ion batteries to address the issues of incompatibility with the conventional electrolytes. These alloying anodes are shown to be compatible with a wide range of conventional electrolytes and are less susceptible to the passivation layer formation.[15,19,20] Among the alloying anodes, Sn appears to be a promising anode because of its high gravimetric capacity, ductility, and low intercalation voltage.[15] A theoretical study by Wang *et al.*[21] indicated that Sn has a relatively low migration barrier for Mg^{2+} ions, making it a competitive anode for RMBs.

Sn exists in two allotropic forms: α- and β-Sn. The ground-state structure of Sn is a face-centered cubic (fcc) with a diamond crystal structure known as a α-Sn phase, which is a zero-gap semiconductor.[22] At a transition temperature of 13 °C, α-Sn transforms into the β-Sn phase, a body-centered tetragonal (bct) metal.[23] Most experimental studies of Sn are based on the β-Sn phase as it is the stable phase at room temperature. The β-Sn structure becomes Mg_2Sn with the fcc structure upon magnesiation.[15]

Significant volume change during charge and discharge is a known issue of Sn.[11,24] The structural distortion due to the volume change leads to poor Coulombic efficiency and rapid capacity degradation.[25] The underlying reasons for how the structural changes hamper electrochemical performance remain unclear. Singh *et al.*[15] indicated that amorphization, accompanied by the structural transformation, hinders a complete extraction of Mg^{2+} from Mg_2Sn, which leads to poor Coulombic efficiency and fast capacity fade. The first step of improving the performance of the Sn anode is to gain an in-depth understanding of the phase transformation process during charge and discharge, which can be used for designing future anode materials.

The aim of this study is to investigate the phase transformation from pure Sn (bct) to Mg_2Sn (fcc) on magnesiation. While the β-Sn and Mg_2Sn are the only two known crystalline phases during the cycling of the Sn anode, no detailed information is available for the transformation from bct to fcc structures. This study investigates the relative thermodynamic stability of the bct to fcc phase at intermediate magnesiation levels. The cluster expansion (CE) method coupled with first-principle density functional theory (DFT) calculations have been proven to predict the structures formed during the battery charging and discharging.[26–28] Previous CE study on Mg–Sn alloys only considers hcp and fcc structures[29] while overlooking the bct structure, which is known to be the most stable phase for pure Sn.[23] The present work is the first theoretical study that includes the missing bct structure in the phase analysis. The hcp phase has not been considered in this study as it is not present during the charge–discharge process of the RMBs. Two CE models are developed to determine the most thermodynamically stable phase at different Mg concentration levels by comparing the formation energies of bct and fcc structures. In addition, we simulated the voltage profile using Monte Carlo (MC) simulations to gain more insights into how the thermodynamic stability of the materials is related to their performance.

II. METHOD

First-principles calculations based on DFT were employed to calculate the total energies of all structures. DFT calculation results are used to train CE models, and all of the calculations were performed using the Vienna *Ab initio* Simulation Package (VASP).[30,31] The Perdew–Burke–Ernzerhof (PBE) parameterized generalized gradient approximation (GGA) functional was employed to describe the exchange and correlation effects, and the projector augmented wave (PAW) method was used to account for the core–valence interactions.[32,33] A plane-wave basis set with a cut-off energy of 520 eV is used for the calculations. The Brillouin zone is integrated with the *k*-point mesh generated using the Monkhorst–Pack scheme with a *k*-point density of 4 per $Å^{-1}$.[34] The convergence threshold for electronic degrees of freedom was 10^{-6} eV, and the interatomic forces were set to 10^{-2} eV $Å^{-1}$ for the structural relaxation.

We developed two separate CE models for α-Sn and β-Sn systems, where both of them are trained using corresponding DFT calculations. For simplicity, we refer to α-Sn and β-Sn systems as fcc and bct structures, respectively, based on their parent lattice structures. The energies from the first-principles calculations were then used to build the CE model to explore the configurational space more effectively. The CLuster Expansion in Atomic Simulation Environment (CLEASE) package was used to generate training structures for DFT calculations and to construct the CE model by fitting the effective cluster interactions (ECIs).[27] The training structures were generated systematically using different generation schemes provided in the CLEASE package. The first set of structures was generated using a random generation method. The subsequent structures are generated to ensure that energetically stable structures are included in the training set while the configurational space is sufficiently explored. Two generation schemes are employed for this work: a probe structure[35,36] scheme was used to generate structures that differ the most from the existing training set in the database and the ground-state structure generation scheme based on simulated annealing was used to include low-energy structures.[37]

A template lattice structure describing the substitutional disorder is needed to construct a CE model. A structure with a space group 216 [shown in Fig. 1(a)] is used to represent fcc structures (α-Sn and Mg_2Sn) as it is the common subgroup with the highest symmetry for the space groups of Mg_2Sn (space group 225) and Sn (space group 227). The structure becomes α-Sn when 4b and 4c Wyckoff positions are occupied by Sn and vacancy, respectively. The Mg_2Sn structure can be realized using the template when 4b and 4c positions are occupied by Mg. The charging procedure can be mimicked by letting the 4b sites be occupied by either Mg or Sn, while the 4c sites are occupied by either Mg or vacancy. A total of 200 structures are generated for the fcc structures while applying the above site constraints. The 200 structures consist of structures with a conventional cell ($1 \times 1 \times 1$ cell consisting of 12 atoms), $2 \times 1 \times 1$ cell (24 atoms), and $2 \times 2 \times 1$ cell (48 atoms).

A template structure with space group 141 was used to construct the CE model for bct structures [shown in Fig. 1(b)] as the β-Sn phase has a bct crystal structure with the space group 141. There is no imposed constraint for the occupation of the lattice sites, which means any of the lattice sites can be occupied by either Mg or Sn. It is known from experiments that the solubility of magnesium in

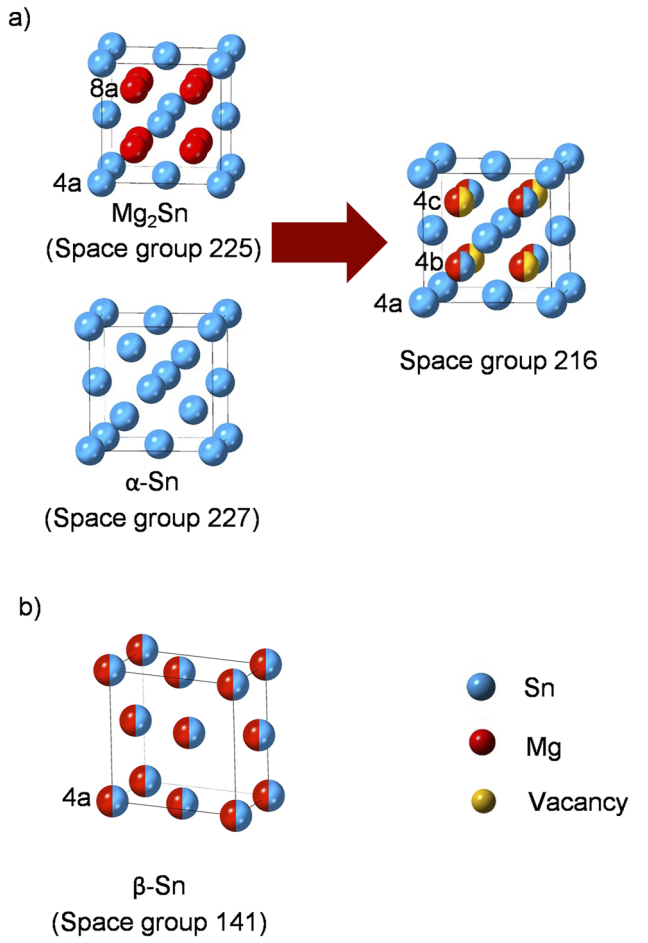

FIG. 1. (a) Structures of Sn and Mg_2Sn, which can be represented using a common template with space group 216. (b) Template with space group 141 for bct structures.

bct Sn is very low.[38,39] Therefore, we limited the magnesiation concentration in the bct structure to be up to 12.5% Mg to allow for a thorough sampling at low Mg concentration. We generated 170 bct structures with the Mg concentration below 12.5% to train the CE model. The CE models for bct and fcc structures were constructed using the maximum cut-off radii of 9, 9, and 7 Å for the two-body, three-body, and four-body clusters, respectively. Two regularization schemes, ℓ_1 and ℓ_2 types, are compared for its predictive power, which is evaluated using leave-one-out cross-validation (LOOCV) score.

One technical issue for constructing an accurate CE model is the large lattice distortion after the structure relaxation, which originates from the presence of vacancies or large mismatch in atomic radii of elements that occupy the lattice. The lattice distortions introduce "noise" in the CE model, which assumes an ideal lattice structure. One strategy to alleviate the issue of lowered accuracy is to eliminate the heavily distorted structures.[29,40,41] The lattice distortion can be quantitatively measured using normalized mean square displacement (NMSD), which is described as[40]

$$\mathrm{NMSD} = \frac{\mathrm{MSD}}{\mathrm{V}^{\frac{2}{3}}}, \tag{1}$$

where V is the volume of the structure and MSD is the mean square displacement calculated using

$$\mathrm{MSD} = \frac{\sum_{\mathrm{atom}} \sum_{X=x,y,z} (X[f] - X[i])^2}{N_{\mathrm{atom}}}. \tag{2}$$

$X[f]$ and $X[i]$ are Cartesian coordinates of the final relaxed structure and initial unrelaxed structure, respectively, and N_{atom} is the total number of atoms in the structure. The structures with a high value of NMSD (i.e., heavily distorted structures) are removed from the training set to construct a CE model without much distortion noise.

Monte Carlo (MC) simulations were performed using the constructed CE model to investigate the relative stability of fcc and bct structures and to obtain the voltage profile.[28,42] We used canonical MC at various fixed concentrations for the phase stability analysis. The lowest energy structure for each concentration was obtained using a simulated annealing technique. The starting temperature of the MC simulations was set to 10^{10} K, which was gradually lowered to 2 K. A $5 \times 5 \times 15$ supercell consisting of 1200 atoms was used for the fcc structures, while a $6 \times 6 \times 9$ supercell consisting of 1296 atoms was used for bct structures.

The relative stability of the phases was investigated using convex-hull analysis. The formation energy for the construction of convex hull is calculated using the following equation:

$$E_f = E_{\mathrm{Mg_xSn}} - X_{\mathrm{Mg}} E_{\mathrm{Mg}} - X_{\mathrm{Sn}} E_{\alpha-\mathrm{Sn}}, \tag{3}$$

where $E_{\mathrm{Mg_xSn}}$ $(0 < x < 2)$ is the total energy of the structure and X_{Mg} and X_{Sn} are the concentration of Mg and Sn in the structure, respectively. E_{Mg} and $E_{\alpha-\mathrm{Sn}}$ are the energy per atom of pure Mg (hcp) and α-Sn, respectively.

The open-circuit voltage (OCV) profile was obtained using semi-grand canonical Monte Carlo (sgcMC) simulations. The sgcMC has the advantage of controlling the concentration of the system by imposing fixed chemical potential. Each trial move in sgcMC simulation consists of selecting a random site and substituting the site with a different element, which makes the concentrations of species in the cell to fluctuate from one point to another. The chosen value of chemical potential controls the average concentration of species. The sgcMC simulations presented in this work require two chemical potential values since there are two binary sub-lattices in the simulation cell that consists of Mg–Sn and Mg–vacancy. Throughout this work, the two sub-lattices were kept in internal equilibrium by constraining the chemical potential of Mg to be the same on both of the two sub-lattices. This constraint allows us to control the Mg concentration by varying one chemical potential. This chemical potential can be directly used to calculate the OCV of the half-cell consisting of Mg and Sn electrodes (the Sn electrode is the material under study, which is magnesiated up to Mg_2Sn). The OCV is calculated using the following formula:

$$\mathrm{OCV} = -\frac{\mu_{\mathrm{Mg}}^{\mathrm{Mg_xSn}} - \mu_{\mathrm{Mg}}}{e}. \tag{4}$$

Here, $\mu_{Mg}^{Mg_xSn}$ $(0 < x < 2)$ is the chemical potential in eV per Mg atom in Mg_xSn (this is the chemical potential obtained from sgcMC), μ_{Mg} is the energy per atom of the pure Mg in the hcp crystal structure calculated as −1.5095 eV, and e is the electric charge, which is 2 for Mg^{2+} ion. The same settings were used for the simulated annealing for the sgcMC simulations, except for the use of a 10 × 10 × 10 supercell consisting of 12 000 atoms for simulating fcc structures. The large supercell was used to allow the system to explore very low magnesium concentrations as a dip in voltage is observed in the experimental voltage profile at low magnesium concentrations.[15]

III. RESULTS AND DISCUSSION

A. Cluster expansion

As the first step of constructing the CE model, the relaxed structures from the DFT simulations are examined to determine their NMSDs to quantitatively investigate their degree of distortion. The lattice distortion of relaxed structures in the considered magnesium range and their distributions are shown in Fig. 2. The Mg concentrations ranging from 0% to ~67% and from 0% to 12.5% are considered for fcc and bct structures, respectively. It is noted that lattice distortion is low in the vicinity of known stable concentrations (α-Sn and Mg_2Sn for fcc structures and β-Sn for bct structures). The heavily distorted structures tend to be present in the concentration ranges that deviate significantly from the known stable structures (i.e., α-Sn, β-Sn and Mg_2Sn). The inclusion of these heavily distorted structures in the training set has been shown to have an adverse effect on the predictive power of the CE model.[29,40] In particular, Nguyen *et al.*[40] demonstrated that the accuracy of the CE model improved when it is trained with structures with the NMSD value of less than 0.1%.[40] Of the 200 fcc and 170 bct structures, 106 fcc and 71 bct structures had the NMSD values below 0.1%.

The effect of filtering out the distorted structures is verified by comparing the performances of the CE models constructed with and without the distorted structures. The performance is measured using the LOOCV score, and the NMSD value of 0.1% is used as a threshold to filter out the distorted structures. The LOOCV score of CE models with and without distorted structures is given in Table I. Two commonly used regularization schemes, ℓ_1- and ℓ_2-regularized fits, are used for obtaining the LOOCV scores. The LOOCV score of the fcc system improved substantially upon the removal of the highly distorted structures; the LOOCV score improved from 24.95 to 6.59 meV/atom for the ℓ_1-regularized fit and from 25.89 to 5.89 meV/atom for the ℓ_2-regularized fit. The improved LOOCV scores agree well with the findings of Nguyen *et al.*[40] The difference in the LOOCV for ℓ_1- and ℓ_2-regularized fits is negligible, and they deliver similar MC simulation results and convex hull diagram. The key difference is in the number of ECIs used in the CE model. The ℓ_1-regularized fit yields a lower number of ECIs, leading to a reduced computational time for the subsequent MC simulations. Consequently, the CE model constructed using the ℓ_1-regularized fit was used for the subsequent MC simulations for the fcc system.

No significant improvement in the LOOCV is found for the bct system upon the removal of the distorted structures. Despite the lack of significant change in the LOOCV score, it is observed that the structures with high NMSD values relax into different space groups. The structures with high NMSD values are discarded from the training set since the relaxed structures no longer correspond to the original lattice model. In other words, we only used the structures in the training set that remain to have the same space group as we specified. It is evident from Table I that the LOOCV score with ℓ_1 regularization is significantly higher than those with ℓ_2 regularization. Hence, the ECIs based on ℓ_2-regularized fit is used for the MC simulation of the bct system.

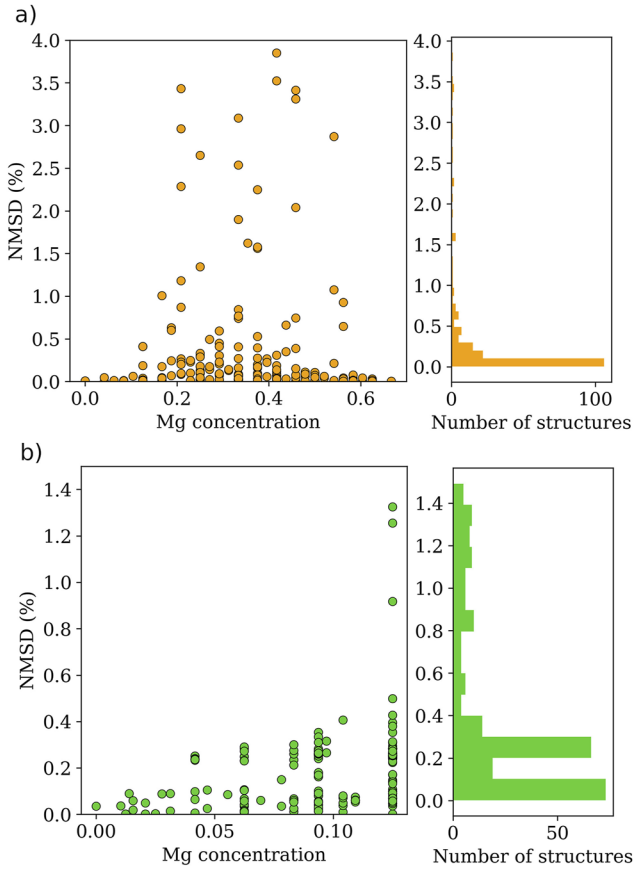

FIG. 2. Distortion of the structures based on the normalized mean square displacement (NMSD) values for the (a) fcc system and (b) bct system.

TABLE I. LOOCV score for the CE models of the fcc and the bct structures before and after removing distorted structures. LOOCV scores with ℓ_1- and ℓ_2-regularized fits are given for all models.

	All structures			Undistorted structures		
	No. structures	LOOCV (meV/atom)		No. structures	LOOCV (meV/atom)	
		ℓ_1	ℓ_2		ℓ_1	ℓ_2
fcc	200	24.95	25.89	106	6.59	5.89
bct	170	13.66	4.39	71	13.31	3.7

B. Convex-hull analysis

The stable structures at different levels of magnesiation are identified through convex-hull analysis. The convex-hull plot obtained from DFT calculations without distorted structures for bct and fcc structures are shown in Fig. 3(a), and the one from the canonical MC based on CE models trained with this DFT dataset is shown in Fig. 3(b). It can be seen from both convex-hull plots that α-Sn (fcc) is more stable than the β-Sn (bct), which agrees with experimental and theoretical studies that α-Sn is the stable phase at low temperatures (temperature below 13 °C).[23,43] Furthermore, the fcc structures are energetically more favorable for the entire magnesiation levels considered. The canonical MC simulation for bct structures predicts a new phase when the Mg concentration is around 11% [Fig. 3(b)]. However, the relative energy of this phase with respect to the fcc is high, which indicates that this phase will not form at low temperatures. Jain *et al.*[44] reported an Mg_9Sn_5 phase to be thermodynamically stable. This phase is not observed in our convex hull since we only considered the structures in space groups 225 and 141. We calculated the formation energy of this structure and observed that this structure falls on the hull line. However, this structure is reported as a high temperature and pressure phase and will not form under normal operating conditions of batteries.[45]

The vibrational contributions should be added to the formation energies to compare the bct and fcc systems at temperatures higher than 0 K. As the phonon calculations using DFT are computationally expensive, we include the vibrational contribution from the study of Legrain and Manzhos[43] on α-Sn and β-Sn based on DFT and the harmonic approximation. They calculated the difference in vibrational contribution to energy between β-Sn and α-Sn at transition temperature to be 0.024 eV/atom. The difference in energy is subtracted from the energies of all the bct structures to include the vibrational contributions effectively. This approximation is valid since our training set consists only of low Mg concentration structures and stays in the original parent lattice after discarding the highly distorted structures.

The convex-hull plots after including the vibrational contributions to DFT and canonical MC results are shown in Figs. 3(c) and 3(d), respectively. The energies of α-Sn and β-Sn become almost the same upon the inclusion of the vibrational contribution corresponding to the transition temperature. The updated convex-hull plots show that Sn and Mg_2Sn are the two stable phases upon

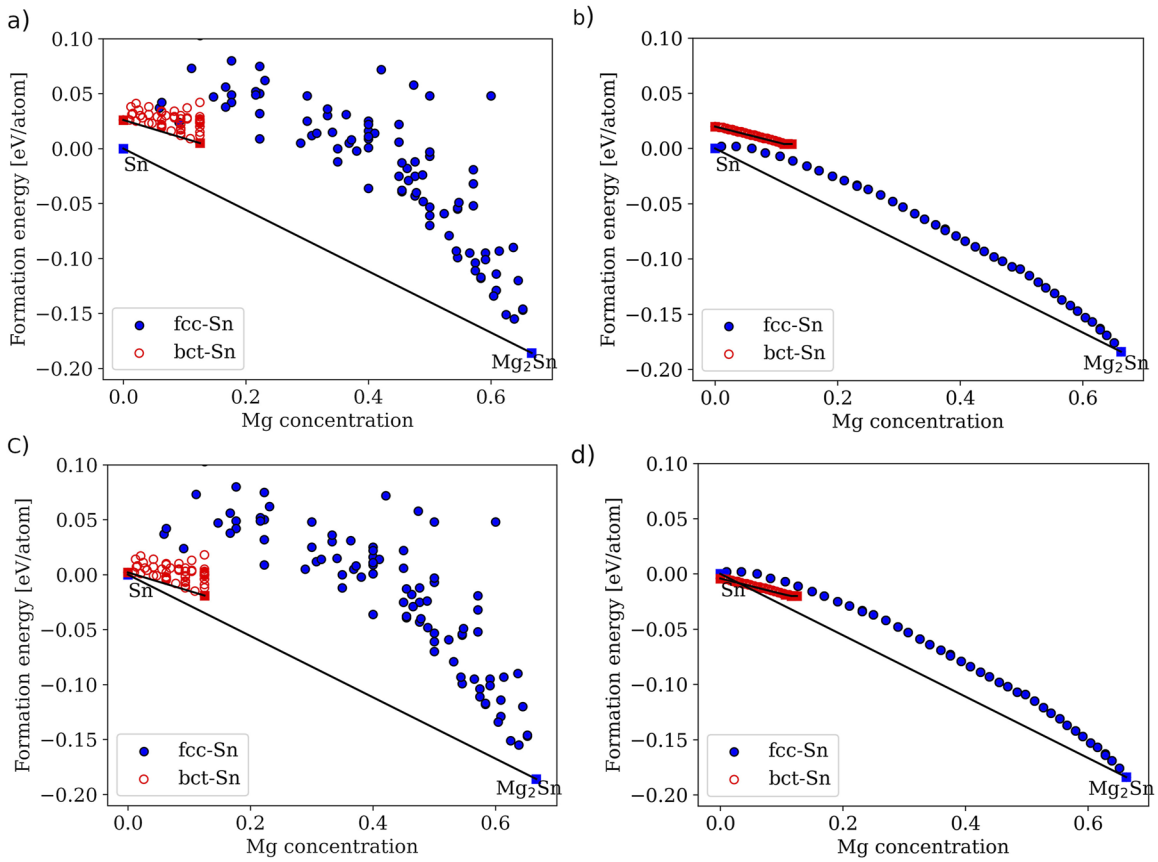

FIG. 3. Convex hull from (a) DFT calculations, (b) canonical MC simulations, and (c) DFT calculations with 0.024 eV/atom subtracted from the energy per atom of bct structures to include the vibrational contribution and (d) canonical MC based on the CE model trained with vibrational contribution added DFT dataset.

alloying Sn with Mg. Furthermore, it can be seen from the convex-hull plots that no other stable intermediate states are present during the charging of the Sn electrode to Mg_2Sn. The energies of fcc and bct structures overlap slightly only when the Mg concentration is very low, and the fcc structures become more stable as the Mg concentration is increased, indicating that bct structures are only stable when the Mg concentration is negligible. The results indicate that the nucleation of Mg_2Sn (fcc) will take place upon adding Mg to β-Sn. Legrain *et al.*[46] showed that low-concentration doping of Mg is unfavorable in both α-Sn and β-Sn, i.e., Mg prefers to segregate when doped in low concentration in these phases. Although doping of Mg is unfavorable in both phases, β-Sn exhibits lower defect formation energy relative to that of α-Sn, indicating that doping in the β-Sn phase is more stable. A similar trend can be observed in the present study as the system at low Mg concentrations is above the hull line [Figs. 3(b) and 3(d)], and the formation energies of low-concentration Mg in β-Sn are lower than those of α-Sn. We only considered the vibration contribution corresponding to the transition temperature 13 °C, but a similar approach can be used to study the phase transformation at higher temperatures. It is worth noting that the energy difference between the α-Sn and β-Sn without any vibrational contribution ($\Delta E_{\alpha-\beta}$) is 0.026 eV/atom in our study. This matches with the $\Delta E_{\alpha-\beta}$ value of 0.02–0.06 eV/atom reported in the previous DFT studies.[43,44] Legrain and Manzhos[43] pointed out that slight changes in the $\Delta E_{\alpha-\beta}$ can lead to a large difference in the transition temperature, and they obtained a $\Delta E_{\alpha-\beta}$ value of 0.04 eV/atom using the GGA functional. The $\Delta E_{\alpha-\beta}$ value of 0.026 eV/atom calculated in the present study is slightly lower than the value reported in their study. A larger $\Delta E_{\alpha-\beta}$ value will result in pushing the formation energies of β-Sn in Fig. 3 upward, making it less stable compared to the α-Sn.

C. Open-circuit voltage profile

The thermodynamic stability of the phases studied using the convex-hull plots is directly related to the voltage profile of batteries. The voltage profile obtained from the sgcMC simulation is shown in Fig. 4. The voltage plateau at 0.15 V obtained from the sgcMC matches the experimental value reported by Singh *et al.*[15] In their results, a slight dip in the voltage was observed at the beginning of magnesiation, which could originate from the kinetics of the bct to fcc transition. Since we only considered the thermodynamics of the phase transformation, the dip is not observed in the simulated voltage profile. The flat voltage profile predicted by the MC simulations indicates that the anode material is phase-separated during charging and discharging.

The magnesium solubility in Sn is low,[38,39] which could be a possible cause of the formation of two phases rather than a solid solution. The flat voltage profile is consistent with the convex-hull analysis, where no phases other than Sn and Mg_2Sn are observed. The single-phase β-Sn becomes phase-separated between β-Sn and Mg_2Sn during charge. At the end of charging, the system becomes a single-phase Mg_2Sn. Some studies suggest that an amorphous phase can form during the transformation from Mg_2Sn to β-Sn upon discharge.[15,47] Some of the highly distorted structures discarded for CE training had low formation energies that lie close to the convex hull, indicating that the system could transform into an intermediate phase (possibly an amorphous phase as indicated in previous

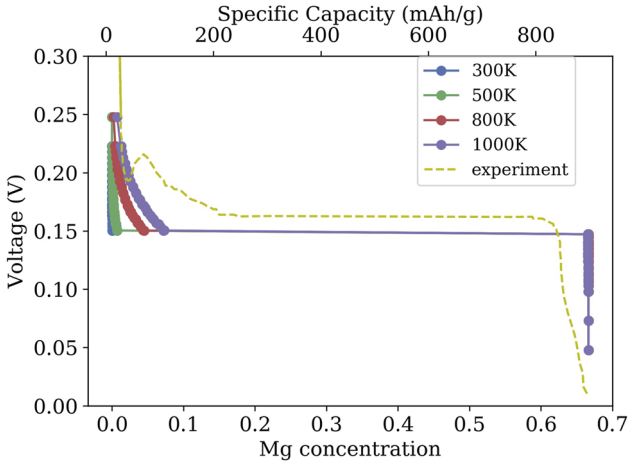

FIG. 4. Voltage profile obtained from the semi-grand canonical MC simulation for fcc structures. The dotted line is the experimental voltage profile from Ref. 15.

experimental studies) during the charging/discharging of the battery. A sufficiently slow discharge process can transform Mg_2Sn to β-Sn without losing its crystallinity. This transformation can happen via two possible routes. The first route is that Mg_2Sn transforms to α-Sn upon demagnesiation as they share a common parent lattice with space group 216 [Fig. 1(a)], followed by a transformation from α-Sn to β-Sn (i.e., $Mg_2Sn \rightarrow \alpha\text{-Sn} \rightarrow \beta\text{-Sn}$). However, it is not clear whether α-Sn to β-Sn transformation is massive or martensitic. Mitchell and Donnelly[48] reported that the α to β transformation is highly likely to be massive in nature due to the absence of a specific orientation relationship. Ojima *et al.*,[49] on the other hand, suggested that the transformation is mainly massive but also martensitic. The discrepancy indicates that a detailed study on the transformation from α-Sn to β-Sn is required. The second route is a direct transformation from the Mg_2Sn structure to β-Sn upon demagnesiation without an intermediate α-Sn (i.e., $Mg_2Sn \rightarrow \beta\text{-Sn}$). As shown in Figs. 3(c) and 3(d), the low-concentration Mg structures in the β-Sn phase has lower formation energies than those in the α-Sn phase, indicating the feasibility of taking the second route of bypassing the α-Sn phase entirely. We performed a DFT calculation to test the thermodynamic feasibility of the direct transformation from Mg_2Sn to β-Sn. A full structure relaxation calculation was carried out on a structure where all the Mg atoms in Mg_2Sn are removed from the cell, followed by a slight rattling of all the atoms. The structure relaxed to a tetragonal crystal structure, which is very similar to pristine β-Sn. The current work focuses on the thermodynamic stability of the phases present during the cycling of the Sn anode in RMBs. Further work on the kinetics of these phases to understand the transformation pathway is under way.

IV. CONCLUSION

We investigated the phase transformation of the Sn anode for RMBs using two DFT-based CE models to analyze the energetics of bct and fcc structures. This is the first time the energetics of fcc and bct phases are evaluated in the same framework to study

the phase transformation in Mg–Sn alloys. We performed canonical MC to obtain the convex-hull plots and sgcMC to obtain the open-circuit voltage profile. The phase stability analysis using the convex-hull plots demonstrates that bct structures are only stable at very low magnesium concentrations. The bct-Sn starts to transform into Mg_2Sn upon magnesiation. The voltage profile obtained from sgcMC simulations shows the voltage plateau that is consistent with the value reported in previous experiments. The flat voltage profile obtained from sgcMC is consistent with the phase stability analysis where the material remains phase-separated between β-Sn and Mg_2Sn during the charging and discharging of the battery. The highly distorted structures discarded in the CE model had low formation energies, suggesting that the material could transform into an amorphous phase during cycling. Our novel approach considers the three possible routes for the transformation from Mg_2Sn to β-Sn in this study. The first route is the transformation via an intermediate α-Sn phase ($Mg_2Sn \rightarrow \alpha$-Sn $\rightarrow \beta$-Sn). The second route is the direct transformation from Mg_2Sn to β-Sn ($Mg_2Sn \rightarrow \beta$-Sn). The third route is via an intermediate amorphous phase ($Mg_2Sn \rightarrow$ amorphous phase $\rightarrow \beta$-Sn). Further study is needed to understand the kinetic barrier and the phase transformation pathways.

ACKNOWLEDGMENTS

The authors thank Piotr Jankowski for fruitful discussions. The authors would like to acknowledge support from the "European Magnesium Interactive Battery Community (e-Magic)" FET-Proactive project (Contract No. 824066). J.M.G.L. acknowledges support from the Villum Foundation's Young Investigator Programme [fourth round, project: *In silico* design of efficient materials for next generation batteries (Grant No. 10096)].

AUTHOR DECLARATIONS

Conflict of Interest

The authors have no conflicts to disclose.

Author Contributions

Smobin Vincent: Conceptualization (equal); Data curation (equal); Formal analysis (equal); Methodology (equal); Writing – original draft (equal); Writing – review & editing (equal). **David Kleiven:** Formal analysis (equal); Methodology (equal); Writing – original draft (equal). **Juan Maria Garcia Lastra:** Conceptualization (equal); Formal analysis (equal); Methodology (equal); Supervision (equal); Writing – original draft (equal); Writing – review & editing (equal). **Jin Hyun Chang:** Conceptualization (equal); Formal analysis (equal); Methodology (equal); Supervision (equal); Writing – original draft (equal); Writing – review & editing (equal).

DATA AVAILABILITY

The data that support the findings of this study are available from the corresponding author upon reasonable request.

REFERENCES

[1] D. Calisaya-Azpilcueta, S. Herrera-Leon, F. A. Lucay, and L. A. Cisternas, "Assessment of the supply chain under uncertainty: The case of lithium," Minerals **10**, 604 (2020).
[2] P. G. Schiavi, P. Altimari, R. Zanoni, and F. Pagnanelli, "Full recycling of spent lithium ion batteries with production of core-shell nanowires//exfoliated graphite asymmetric supercapacitor," J. Energy Chem. **58**, 336–344 (2021).
[3] B. Bustos-Gallardo, G. Bridge, and M. Prieto, "Harvesting lithium: Water, brine and the industrial dynamics of production in the Salar de Atacama," Geoforum **119**, 177–189 (2021).
[4] S. Kosai, U. Takata, and E. Yamasue, "Natural resource use of a traction lithium-ion battery production based on land disturbances through mining activities," J. Cleaner Prod. **280**, 124871 (2021).
[5] R. Shah, V. Mittal, E. Matsil, and A. Rosenkranz, "Magnesium-ion batteries for electric vehicles: Current trends and future perspectives," Adv. Mech. Eng. **13**, 16878140211003398 (2021).
[6] F. Bella, S. De Luca, L. Fagiolari, D. Versaci, J. Amici, C. Francia, and S. Bodoardo, "An overview on anodes for magnesium batteries: Challenges towards a promising storage solution for renewables," Nanomaterials **11**, 810 (2021).
[7] P. Saha, M. K. Datta, O. I. Velikokhatnyi, A. Manivannan, D. Alman, and P. N. Kumta, "Rechargeable magnesium battery: Current status and key challenges for the future," Prog. Mater. Sci. **66**, 1–86 (2014).
[8] T. Ichitsubo, T. Adachi, S. Yagi, and T. Doi, "Potential positive electrodes for high-voltage magnesium-ion batteries," J. Mater. Chem. **21**, 11764–11772 (2011).
[9] H. D. Yoo, S.-D. Han, I. L. Bolotin, G. M. Nolis, R. D. Bayliss, A. K. Burrell, J. T. Vaughey, and J. Cabana, "Degradation mechanisms of magnesium metal anodes in electrolytes based on $(CF_3SO_2)_2N^-$ at high current densities," Langmuir **33**, 9398–9406 (2017).
[10] D. Aurbach, Z. Lu, A. Schechter, Y. Gofer, H. Gizbar, R. Turgeman, Y. Cohen, M. Moshkovich, and E. Levi, "Prototype systems for rechargeable magnesium batteries," Nature **407**, 724–727 (2000).
[11] J. Niu, Z. Zhang, and D. Aurbach, "Alloy anode materials for rechargeable Mg ion batteries," Adv. Energy Mater. **10**, 2000697 (2020).
[12] Z. Ma, D. R. MacFarlane, and M. Kar, "Mg cathode materials and electrolytes for rechargeable Mg batteries: A review," Batteries Supercaps **2**, 115–127 (2019).
[13] T. D. Gregory, R. J. Hoffman, and R. C. Winterton, "Nonaqueous electrochemistry of magnesium: Applications to energy storage," J. Electrochem. Soc. **137**, 775 (1990).
[14] S. Vincent, J. H. Chang, and J. M. Garcia Lastra, "Computational design of ductile magnesium alloy anodes for magnesium batteries," Batteries Supercaps **4**, 522–528 (2021).
[15] N. Singh, T. S. Arthur, C. Ling, M. Matsui, and F. Mizuno, "A high energy-density tin anode for rechargeable magnesium-ion batteries," Chem. Commun. **49**, 149–151 (2013).
[16] F. Murgia, E. T. Weldekidan, L. Stievano, L. Monconduit, and R. Berthelot, "First investigation of indium-based electrode in Mg battery," Electrochem. Commun. **60**, 56–59 (2015).
[17] K. Periyapperuma, T. T. Tran, M. I. Purcell, and M. N. Obrovac, "The reversible magnesiation of Pb," Electrochim. Acta **165**, 162–165 (2015).
[18] A. Benmayza, M. Ramanathan, N. Singh, F. Mizuno, and J. Prakash, "Electrochemical and thermal studies of bismuth electrodes for magnesium-ion cells," J. Electrochem. Soc. **162**, A1630 (2015).
[19] T. S. Arthur, N. Singh, and M. Matsui, "Electrodeposited Bi, Sb and $Bi_{1-x}Sb_x$ alloys as anodes for Mg-ion batteries," Electrochem. Commun. **16**, 103–106 (2012).
[20] Y. NuLi, J. Yang, J. Wang, and Y. Li, "Electrochemical intercalation of Mg^{2+} in magnesium manganese silicate and its application as high-energy rechargeable magnesium battery cathode," J. Phys. Chem. C **113**, 12594–12597 (2009).
[21] Z. Wang, Q. Su, J. Shi, H. Deng, G. Q. Yin, J. Guan, M. P. Wu, Y. L. Zhou, H. L. Lou, and Y. Q. Fu, "Comparison of tetragonal and cubic tin as anode for Mg ion batteries," ACS Appl. Mater. Interfaces **6**, 6786–6789 (2014).
[22] S. Groves and W. Paul, "Band structure of gray tin," Phys. Rev. Lett. **11**, 194 (1963).
[23] G. A. Busch and R. Kebn, "Semiconducting properties of gray tin," Solid State Phys. **11**, 1–40 (1960).

[24]O. I. Malyi, T. L. Tan, and S. Manzhos, "In search of high performance anode materials for Mg batteries: Computational studies of Mg in Ge, Si, and Sn," J. Power Sources **233**, 341–345 (2013).
[25]D.-T. Nguyen, X. M. Tran, J. Kang, and S.-W. Song, "Magnesium storage performance and surface film formation behavior of tin anode material," ChemElectroChem **3**, 1813–1819 (2016).
[26]J. H. Chang, C. Baur, J.-M. Ateba Mba, D. Arčon, G. Mali, D. Alwast, R. J. Behm, M. Fichtner, T. Vegge, and J. M. Garcia Lastra, "Superoxide formation in Li_2VO_2F cathode material – A combined computational and experimental investigation of anionic redox activity," J. Mater. Chem. A **8**, 16551–16559 (2020).
[27]J. H. Chang, D. Kleiven, M. Melander, J. Akola, J. M. Garcia-Lastra, and T. Vegge, "CLEASE: A versatile and user-friendly implementation of cluster expansion method," J. Phys.: Condens. Matter **31**, 325901 (2019).
[28]Y. S. Meng and M. E. Arroyo-de Dompablo, "First principles computational materials design for energy storage materials in lithium ion batteries," Energy Environ. Sci. **2**, 589–609 (2009).
[29]K. Wang, D. Cheng, C.-L. Fu, and B.-C. Zhou, "First-principles investigation of the phase stability and early stages of precipitation in Mg–Sn alloys," Phys. Rev. Mater. **4**, 013606 (2020).
[30]G. Kresse and J. Furthmüller, "Efficiency of ab-initio total energy calculations for metals and semiconductors using a plane-wave basis set," Comput. Mater. Sci. **6**, 15–50 (1996).
[31]G. Kresse and J. Furthmüller, "Efficient iterative schemes for *ab initio* total-energy calculations using a plane-wave basis set," Phys. Rev. B **54**, 11169–11186 (1996).
[32]J. P. Perdew, K. Burke, and M. Ernzerhof, "Generalized gradient approximation made simple," Phys. Rev. Lett. **77**, 3865–3868 (1996).
[33]P. E. Blöchl, "Projector augmented-wave method," Phys. Rev. B **50**, 17953–17979 (1994).
[34]H. J. Monkhorst and J. D. Pack, "Special points for Brillouin-zone integrations," Phys. Rev. B **13**, 5188 (1976).
[35]A. Seko, Y. Koyama, and I. Tanaka, "Cluster expansion method for multicomponent systems based on optimal selection of structures for density-functional theory calculations," Phys. Rev. B **80**, 165122 (2009).
[36]A. Seko and I. Tanaka, "Cluster expansion of multicomponent ionic systems with controlled accuracy: Importance of long-range interactions in heterovalent ionic systems," J. Phys.: Condens. Matter **26**, 115403 (2014).
[37]A. van de Walle and G. Ceder, "Automating first-principles phase diagram calculations," J. Phase Equilib. **23**, 348–359 (2002).
[38]A. A. Nayeb-Hashemi and J. B. Clark, "The Mg–Sn (magnesium–tin) system," Bull. Alloy Phase Diagrams **5**, 466–476 (1984).
[39]A. Nayak and W. Oelsen, "Quantitative thermal analysis of magnesium–tin alloys by calorimetric measurement for the determination of solidus and liquidus curves," Trans. Indian Inst. Met. **22**, 53–58 (1969).
[40]A. H. Nguyen, C. W. Rosenbrock, C. S. Reese, and G. L. Hart, "Robustness of the cluster expansion: Assessing the roles of relaxation and numerical error," Phys. Rev. B **96**, 014107 (2017).
[41]A. van de Walle, "Multicomponent multisublattice alloys, nonconfigurational entropy and other additions to the Alloy Theoretic Automated Toolkit," CALPHAD: Comput. Coupling Phase Diagrams Thermochem. **33**, 266–278 (2009).
[42]A. Van der Ven and G. Ceder, "Ordering in $Li_x(Ni_{0.5}Mn_{0.5})O_2$ and its relation to charge capacity and electrochemical behavior in rechargeable lithium batteries," Electrochem. Commun. **6**, 1045–1050 (2004).
[43]F. Legrain and S. Manzhos, "Understanding the difference in cohesive energies between alpha and beta tin in DFT calculations," AIP Adv. **6**, 045116 (2016).
[44]A. Jain, S. P. Ong, G. Hautier, W. Chen, W. D. Richards, S. Dacek, S. Cholia, D. Gunter, D. Skinner, G. Ceder, and K. A. Persson, "Commentary: The Materials Project: A materials genome approach to accelerating materials innovation," APL Mater. **1**, 011002 (2013).
[45]K.-J. Range, G. H. Grosch, and M. Andratschke, "Studies on AB_2-type intermetallic compounds. Part V[1]. The crystal structure of Mg_9Sn_5, a supposed high-pressure modification of Mg_2Sn," J. Alloys Compd. **244**, 170–174 (1996).
[46]F. Legrain, O. I. Malyi, C. Persson, and S. Manzhos, "Comparison of alpha and beta tin for lithium, sodium, and magnesium storage: An *ab initio* study including phonon contributions," J. Chem. Phys. **143**, 204701 (2015).
[47]D.-T. Nguyen and S.-W. Song, "Magnesium stannide as a high-capacity anode for magnesium-ion batteries," J. Power Sources **368**, 11–17 (2017).
[48]D. R. G. Mitchell and S. E. Donnelly, "A transmission electron microscopy study of the $\beta \rightarrow \alpha$-phase transformation of tin," Philos. Mag. A **63**, 747–755 (1991).
[49]K. Ojima, Y. Taneda, and A. Takasaki, "Direct observation of $\alpha \rightarrow \beta$ transformation in tin by transmission electron microscopy," Phys. Status Solidi A **139**, 139–144 (1993).